Synergic use of two-dimensional materials to tailor interfaces in large area perovskite modules

S. Pescetelli[1§], A. Agresti[1*§], S. Razza[1], H. Pazniak[2], L. Najafi,[3] F. Bonaccorso[3], A. Di Carlo[1,4,*]*

[1]CHOSE, Centre for Hybrid and Organic Solar Cells, University of Rome Tor Vergata, via del Politecnico 1, 00133 Roma, Italy

[2]Faculty of Physics and Center for Nanointegration Duisburg-Essen, University of Duisburg-Essen, Germany

[3]BeDimensional S.p.A., Lungotorrente Secca, 30R, 16163, Genova, Italy

[4]Istituto di Struttura della Materia, CNR-ISM, via del fosso del cavaliere 100, 00133 Roma, Italy

§: Both authors contributed equally to this work

Corresponding Authors

*Sara Pescetelli: pescetel@uniroma2.it,
*Antonio Agresti: antonio.agresti@uniroma2.it,
*Aldo Di Carlo: aldo.dicarlo@uniroma2.it
Author Orcid:
Pescetelli Sara 0000-0002-3336-2425
Agresti Antonio 0000-0001-6581-0387
Di Carlo Aldo 0000-0001-6828-2380

Abstract

In the field of halide perovskite solar cells (PSCs), interface engineering has been conceptualized and exploited as a powerful mean to improve solar cells performances, stability, and scalability.
In this regard, here we propose the use of a multi two-dimensional (2D) material as intra and inter layers in a mesoscopic PSC. By combining graphene into both compact and mesoporous TiO_2, $Ti_3C_2T_x$ MXenes into the perovskite absorbing layer and functionalized-MoS_2 at the interface between perovskite and the hole transporting layer, we boost the efficiency of PSCs (*i.e.*, +10%) compared to the 2D materials-free PSCs. The optimized 2D materials-based structure has been successful extended from lab-scale cell dimensions to large area module on 121 cm^2 substrates (11×11 cm^2) till to 210 cm^2 substrates (14.5×14.5 cm^2) with active area efficiency of 17.2 % and 14.7 %, respectively. The remarkable results are supported by a systematic statistical analysis, testifying the effectiveness of 2D materials interface engineering also on large area devices, extending the 2D materials-perovskite photovoltaic technology to the industrial exploitation.

Keywords: Perovskite-based photovoltaic**,** Perovskite solar cells, Two-dimensional (2D) materials, Interface engineering, Large area perovskite modules.

List of acronymous and abbreviations

Abbreviation	*Definition*
2D	Two-dimensional
30 NR-D	Mesoporous transparent titania paste
AcAc	Acetyl acetone
ACN	Acetonitrile
CB	Chlorobenzene
CE	Counter-Electrode
CsI	Cesium Iodide
$cTiO_2$	Compact TiO_2 layer
DMF	Dimethylformamide
DMSO	Dimethyl Sulfoxide
EQE	External Quantum Efficiency
ETL	Electron Transport Layer
EtOH	Ethanol
FAI	Formamidinium iodide
FF	Fill Factor
f-MoS_2	Functionalized exfoliated zero-dimensional molybdenum disulphide
FTO	Fluorine-doped Tin Oxide
GB	Grain Boundary
HOMO	Highest Occupied Molecular Orbital
HTL	Hole Transport Layer
IE	Interface Engineering
IPA	Isopropanol
IPCE	Incident Photon to Current Efficiency
I-V	Current-Voltage
J_{SC}	Short Circuit Current Density
LG	Low band Gap
Li-TFSI	Lithium bis(trifluoromethanesulfonyl)imide
LPE	Liquid phase exfoliation
LUMO	Lowest Unoccupied Molecular Orbital
MABr	Methylammonium bromide
MPA	Thiol group of 3-mercaptopropionic acid
MPA	3-mercaptopropionic acid
MPP	Maximum Power Point
$mTiO_2$	Mesoporous TiO_2 layer
MXenes	Two-dimensional transition metal carbides/nitride
n-i-p	n-doped layer / intrinsic layer / p-doped layer
NMP	N-methyl-2-pyrrolidone
$PbBr_2$	Lead(II) Bromide
PbI_2	Lead(II) Iodide
PCE	Power Conversion Efficiency
PE	Photo Electrode
P_{inc}	Light incident power
PL	Photoluminescence
PSCs	Perovskite Solar Cells

PSM	Perovskite Solar Module
PTAA	Poly(triarylamine) (PTAA)
RMSE	root mean square error
T	Toluene
tBP	tert-butylpyridine
$Ti(AcAc)_2$	Diisopropoxytitanium bis(acetylacetonate)
TPC	Transient Photocurrent
TPV	Transient Photovoltage
TTIP	titanium(IV) isopropoxide
V_{OC}	Open Circuit Voltage
WF	Work Function

1. Introduction

Among a broad range of photovoltaic (PV) devices, perovskite solar cells (PSCs) are currently sitting in the spotlight due to their simple, cost-effective fabrication procedure and high-power conversion efficiency (PCE). Within a decade of intense global research efforts devoted to the PSC optimization, the best obtained PCE value has now exceeded 25%, making PSC progresses the fastest in the PV technology history.[1] However, despite the quick increase in record efficiency, some crucial challenges remain to be solved to speed-up the commercialization of this cutting-edge technology. The main issues include, but not limited to, the instability under prolonged thermal and light-soaking tests, hysteresis and scalability.[2–7]

Moreover, considering the multilayer structure of PSCs, in which the perovskite absorbing layer is sandwiched between charge selective layers, it is evident the fundamental role of interfaces in designing efficient and stable devices. In fact, recombination at interfaces as well as at grain boundary (GB) inside the perovskite film, badly affect some photovoltaic parameters such as open circuit voltage (V_{OC}) and fill factor (FF), eventually reducing device efficiency[8] and stability.[9]

Thus, particular care should be taken when making junction between perovskite and both electron transport layer (ETL) and hole transport layer (HTL), to minimize the interfacial recombination and at same time to promote fast charge extraction. In fact, charge transfer at the interfaces, interface band alignment, interfacial vacancies, defects due to poor adhesion between layers and energy barriers have a strongly impact on the device performances.[10] Therefore, in the PSC field, interface engineering (IE) approach has recently gained a pivotal role in designing efficient and stable devices by employing graphene and 2D materials, as successfully demonstrated for mesoscopic n-i-p structure.[11–16]

In this contest, the unique morphological, chemical, and optical properties of 2D materials[17] promoted their use as alternative materials to the state of art, not only to enhance the cell performance, but also to improve device scalability by ensuring reproducible results.[18–20] Furthermore, 2D materials are also considered as game-changer in the (photo)chemically/thermal stabilization of perovskite solar devices.[21] More in detail, based on our previous experience, 2D materials have been established either in form of additives for both the photoactive perovskite[22,23] and the charge transporting materials,[19,24,25]or as interfacial layers to foster the injection/transport of the photogenerated charges towards the electrodes, while hindering interfacial charge recombination.[26]

The engineering of the layered structure composing the PSCs involved the use of single-/few-layer graphene flakes as conductive dopants for the ETL, both for compact ($cTiO_2$) and mesoporous TiO_2 ($mTiO_2$). As reported in our previous works, the graphene flake ink[24] enhances the electrical conductivity of the TiO_2, by improving the electron extraction towards the negative electrode.[24]

At the same time, graphene flakes participate in the perovskite crystal growth over mesoscopic scaffolds, significantly improving the crystalline quality of the active material.[12]
The IE strategy for the layered structure composing the PSCs involves behind graphene, a large number of 2D materials from metals to semiconductors and insulators[27,28] that can be produced on-demand and dispersed in several solvents making them suitable for printing process deposition when considering large-area fabrication.[29]
Moreover, the existing broad range of 2D materials can be further extended by tailoring their electronic structure (i.e. Work Function (WF)[30] or band gap), with different chemical functionalizations (such as: small molecules, metal nanoparticles, self-assembled monolayers, ionic liquids and polymers).[31–33] Following this approach, we recently demonstrated the use of chemically functionalized exfoliated zero-dimensional MoS_2 ($fMoS_2$) flakes as interlayer at perovskite/HTL interface for the mesoscopic structure. The resulting effect consisted in a more efficient hole injection/collection at the counter-electrode (CE) with an improved hole dynamics,[34] compared to the unfunctionalized MoS_2 flakes.[35] In fact, the chemical functionalization of MoS_2 by a thiol group of 3-mercaptopropionic acid (MPA)[25] allowed to passivate the lattice defects of the MoS_2[36,37] and to shift the MoS_2 energy bands up, by aligning the valence band edge of MoS_2 with the HOMO level of the perovskite.[34]
Following the new advances in the IE, a new class of 2D materials, namely the transition metal carbides, nitrides and carbonitrides (MXenes) have been successfully used, as doping material in the perovskite adsorber layer, to tune WF without affecting other optoelectronic properties such as band gap and optical absorption.[23,38] In this respect, MXenes represent one of the most promising and effective way for the material WF tuning. In fact, since the surface terminations can be tailored during the MXene synthesis, their electronic structures and eventually their WF can be finely tuned, underlining their powerful role in modern optoelectronics and photovoltaics.
MXenes have been firstly used into perovskite absorber layer to increase the grain size of the film achieving a +12% enhancement in efficiency.[39] A similar enhancement was demonstrated by embedding a small percentage of $Ti_3C_2T_x$ MXene nanosheets into a SnO_2 nanocomposite used as ETL in planar PSCs.[40] Based on our previous experience, the versatility of $Ti_3C_2T_x$ MXene has been demonstrated as interlayer at perovskite/ETL interface as well as dopant for the perovskite absorber. [22,23] More in detail, despite 2D materials IE has been demonstrated to be suitable for PSC, the WF tunability using GRMs is quite limited to values around 4 eV, effectively restricting their applicability. On the contrary, in the case of MXenes the WF could be tune by choosing the proper transition metal as well as the X element in a wide range varying from 1.6 eV (for OH-termination) to 6.25 eV (for O-termination). Such compositional tunability provides a powerful tool to achieve the correct energy band alignment within the device. The main effects of this innovative strategy reflected on perovskite WF modification and interface optimization leading to an enhancement of charge transfer and consequently to a huge improvement in PCE (+26%).[23]
Moreover, the beneficial role of 2D materials is not limited to an improvement of the electrical performances, but also involves scalability and stability.[41]
So far the use of MXenes has been limited to small area devices, however the possibility to use this 2D material for scaling the solar cell to module size will directly impact on the PSC technology exploitation at industrial level. At the same time, a powerful approach consists in combining MXenes with other 2D materials to improve the overall performance of the system, surpassing the performances of MXenes-based PSCs
The present work tries to fill this gap. A smart use of several 2D materials with customized optoelectronic properties is proposed for engineering layer interfaces in a mesoscopic n-i-p cells. In particular, we designed a full 2D materials-perovskite structure consisting in a mixed-cation halide perovskite active layer doped with MXenes and sandwiched between a graphene-modified

mesoscopic ETL and a zero-dimensional $fMoS_2$-based interlayer favouring hole injection into the HTL. We show that such configuration is optimized in term of performance at both cell and large module size, achieving efficiency of 17.2 % and 14.7 % on active area module of ~83 cm^2 and ~137 cm^2, respectively. This demonstrates the pivotal role of the wide 2D material library in the optimization of perovskite PV technology.

2. Materials and methods

2.1 Materials: All the materials were used as received, unless specified otherwise. Mesoporous transparent titania paste (30 NR-D), formamidinium iodide (FAI) and methylammonium bromide (MABr) were purchased from GreatCell Solar. Lead(II) iodide (PbI_2), lead(II) bromide ($PbBr_2$) were purchased from TCI and cesium iodide (CsI) from GmbH. Molybdenum disulphide (MoS_2) crystal was purchased from HQGraphene, while poly(triarylamine) (PTAA) Medium Mw: 20 – 75 kDa (SOL2426M) from Solaris Chem. All other materials, including titanium(IV) isopropoxide (TTIP), diisopropoxytitanium bis(acetylacetonate) ($Ti(AcAc)_2$), acetyl acetone (AcAc), lithium bis(trifluoromethanesulfonyl)imide (Li-TFSI), ethanol (EtOH), isopropanol (IPA), acetone, dimethylformamide (DMF), dimethyl sulfoxide (DMSO), acetonitrile (ACN), tert-butylpyridine (tBP), chlorobenzene (CB), toluene (T), N-methyl-2-pyrrolidone (NMP), 3-mercaptopropionic acid (MPA) and graphite flakes were purchased from Sigma-Aldrich. The graphene flakes ink in EtOH (≥99.8 %) (concentration of 0.9 $mg\,mL^{-1}$) was prepared by liquid phase exfoliation (LPE) of graphite flakes (Sigma–Aldrich) in NMP and exchanged into EtOH (see our previous paper for further details).[12,24,34,42]The functionalized MoS_2 ($fMoS_2$) flakes ink in IPA (concentration of 0.2 $mg\,mL^{-1}$) was produced by chemical functionalization of MoS_2 flakes with MPA (≥ 99%, Sigma Aldrich) (see our previous paper for further details).[12,24,34,42] The single-layer $Ti_3C_2T_x$ nanosheet (Mxenes), consisting of two carbon atoms that bind three titanium ones as elementary units, are produced by chemical etching and exfoliation by sonication (see our previous paper for further details).[23] A complete characterization of the graphene ink used to dope both $cTiO_2$ and $mTiO_2$ layers, the MXenes and the $fMoS_2$ is provided in our previous publication.[23,24,34]

2.2 Device fabrication methods: The device fabrication processing began with the P1 laser patterning of the FTO substrates (FTO, Pilkington, $7\Omega\square^{-1}$). A Nd:YVO4 UV (355nm) pulsed laser system was used to perform single scribes with a pulse fluency of 700 $mJ{\cdot}cm^{-2}$ and a pulse repetition rate of 80 kHz. The pre-patterned FTO substrates were first wiped with detergent and then cleaned by sonication for 10 min in deionized water, acetone, and 2-propanol sequentially. After drying under an air stream, the substrates were cleaned by UV/ozone treatment for 20 min. Then, the substrate was deposited 50 nm layer of $cTiO_2$ film by spry pyrolysis a solution of acetylacetone (1 mL), titanium diisopropoxide (1.5 mL) and ethanol (22.5 mL) at 460 °C. The subsequent step of small area (and large area) device fabrication consists in a thin mesoporous TiO_2 ($mTiO_2$) film (~130 nm) deposited by spin coating. The TiO_2 paste (Dyesol 30 NRD paste diluted in ethanol 1:5 in wt.) was spun at 3000 rpm for 20 s (2000 rpm for 20 s) and followed by the subsequent sintering at 480 °C for 30 min in air. The analogous graphene doped solutions, $cTiO_2$+G and $mTiO_2$+G, are obtained by doping with 1 vol% of graphene ink (from IIT) the pristine solution. Then the substrates were transferred into a N2 glove box. The perovskite films were deposited combining a one-step deposition with antisolvent method. The precursor solution, composed by a mix of FAI (1 M), PbI_2 (1.1 M), MABr (0.2 M), $PbBr_2$ (0.2 M) and CsI (1.5 mM) dissolved in a mixture of anhydrous DMF/DMSO (4:1 vol/vol) was stirred at room temperature for 30 min, and then spin coated onto the samples (70 μL). The precursor solution was spin-coated on the sample with a two steps program at 1000 and 5000 rpm for 10 s and 30 s respectively (1000 and 4000 rpm

for 10 s and 30 s). During the second step, 200 µL (1,5 ml) of CB were poured on the spinning substrate 7 s prior to the end of the program. The resulting film was annealed at 100 °C for 1 h. $fMoS_2$ active buffer layer was deposited onto the perovskite layer by spraying the $fMoS_2$ 0.5 mL (3mL) dispersion in IPA by an airbrush onto the 80 °C pre-heated substrate. The PTAA solution (10 mg mL^{-1} in chlorobenzene) was prepared with the addition of 7 µL of 4-tert-butylpyridine (tBP). and 10 µL of Li-TFSI (170 mg mL^{-1} in acetonitrile). 70 µL (1mL) of as prepared PTAA solution was spin coated on each sample at 3000 rpm for 30 s (2000 rpm for 30s). The entire stuck of each module was patterned by a two-step P2 process made with the same Nd:YVO4 UV (355nm) pulsed laser system, by using a pulse fluency of 248.8 $mJ \cdot cm^{-2}$ and a pulse repetition rate of 80 kHz. In this case the obtained raster scanning distance is 2µm and the width of the ablated area is 400 µm, achieved performing two consecutive ablations made by scribes with a rast scanning distance (RSD) of 2 µm and a width of 13 µm. Finally, the Au electrode (150 nm) was deposited by thermal evaporation under a pressure of about 10^{-6} mBar. The deposition rate was controlled at 0.03 nm s^{-1} in the beginning. After 20 nm of Au layer was deposited, the deposition rate was increased to 0.10 nm s^{-1} by increasing the evaporation power. To get an electrical separation between the module sub-cells counter electrodes, we performed a P3 laser process on the gold layer. The ablations, consisting in a scribe width of 13 µm and an RSD of 3 µm, was obtained by using a fluence of 306 $mJ \cdot cm^{-2}$. The modules aperture ratio is 82%, achieved by considering that a cell width of 9 mm and a dead area of 2 mm.

2.3 Electro-Optical measurements: UV-Vis, PL, IPCE, ARKEO, I-V characteristics.

The UV-Vis absorption spectra of the perovskite layer were recorded using UV-Vis 2550 spectrophotometer from Shimadzu. The spectra were collected using a scan rate of 480nm min^{-1} and a resolution of 1 nm.[43]

Steady state PL measurements were performed with a commercial apparatus (Arkeo – Cicci Research s.r.l.) composed by a 0.3 meter focal length spectrograph with a photon counting unit. The substrates were excited by a green (532 nm) laser at 45° of incidence with a circular spot diameter of 1 mm. The optical coupling system is composed by a lens condenser and a long pass filter.

The PL spectra have been elaborated by an in-house developed Matlab script. In detail, perovskite emission spectra have been fitted by employing the best fitting between single, double, or triple exponential Gaussian line-shape by minimizing the RMSE (root mean square error).

Current-Voltage (I-V) characteristics of masked and encapsulated devices were acquired in air by using a solar simulator (ABET Sun 2000, class A) calibrated at AM1.5 and 100 mW cm^{-2} illumination with a certified reference Si Cell (RERA Solutions RR-1002).[44,45] Incident power was measured with a Skye SKS 1110 sensor. The class was measured with a BLACK-Comet UV–vis spectrometer.

Both reverse and forward I-V scans were performed by using a scan rate of 20mV s^{-1} and 100 mVs^{-1} for masked small-area PSCs and unmasked large-area PSMs, respectively.

Illumination intensity dependence of V_{OC} and dark I-V measurements were performed with a modular testing platform (Arkeo - Cicci research s.r.l.) composed by a white LED array (4200Kelvin) tunable up to 200 mW cm^{-2} of optical power density and a high-speed source meter unit (600 Ksamples s^{-1}) in a four-wire configuration. A spring contact-based sample holder was used to improve the repeatability of the experiments. Transient measurements were performed in a high perturbation configuration by acquiring the entire V_{OC} rise profile after switching the light intensity from 0 to 1 Sun.

Incident Photon to current Conversion Efficiency (IPCE) spectra acquisitions were carried out by means of a homemade setup composed by a monochromator (Newport, mod. 74000) coupled with a

xenon lamp (Oriel Apex, Newport) and a source meter (Keithley, mod. 2612). A homemade LabVIEW program controlled the spectra acquisition.

3. Results and discussion

3.1 Small-area devices

The four different tested structures are reported in **Fig. 1** together with the relative energy band diagram. Starting from the reference (PSC-ref) that does not contain 2D materials, we progressively introduce 2D materials in different parts of the devices: PSC-G consists in only graphene-modified ETL structure (**Fig. 1b**); PSC-G/MX is obtained adding also the MXenes into the perovskite active layer (**Fig 1c**), while PSC-G/MX/fMoS$_2$ considers also a fMoS$_2$ interlayer between perovskite absorber and the PTAA HTL (**Fig. 1d**). The full 2D engineered PSC (**Fig. 1d**) is designed to progressively improve the alignment of the energy bands. The detailed description of the PSC manufacturing is reported in Materials and Methods section, while a detailed description of the impact of the 2D materials in the perovskite devices based on our previous studies is reported in S.I.

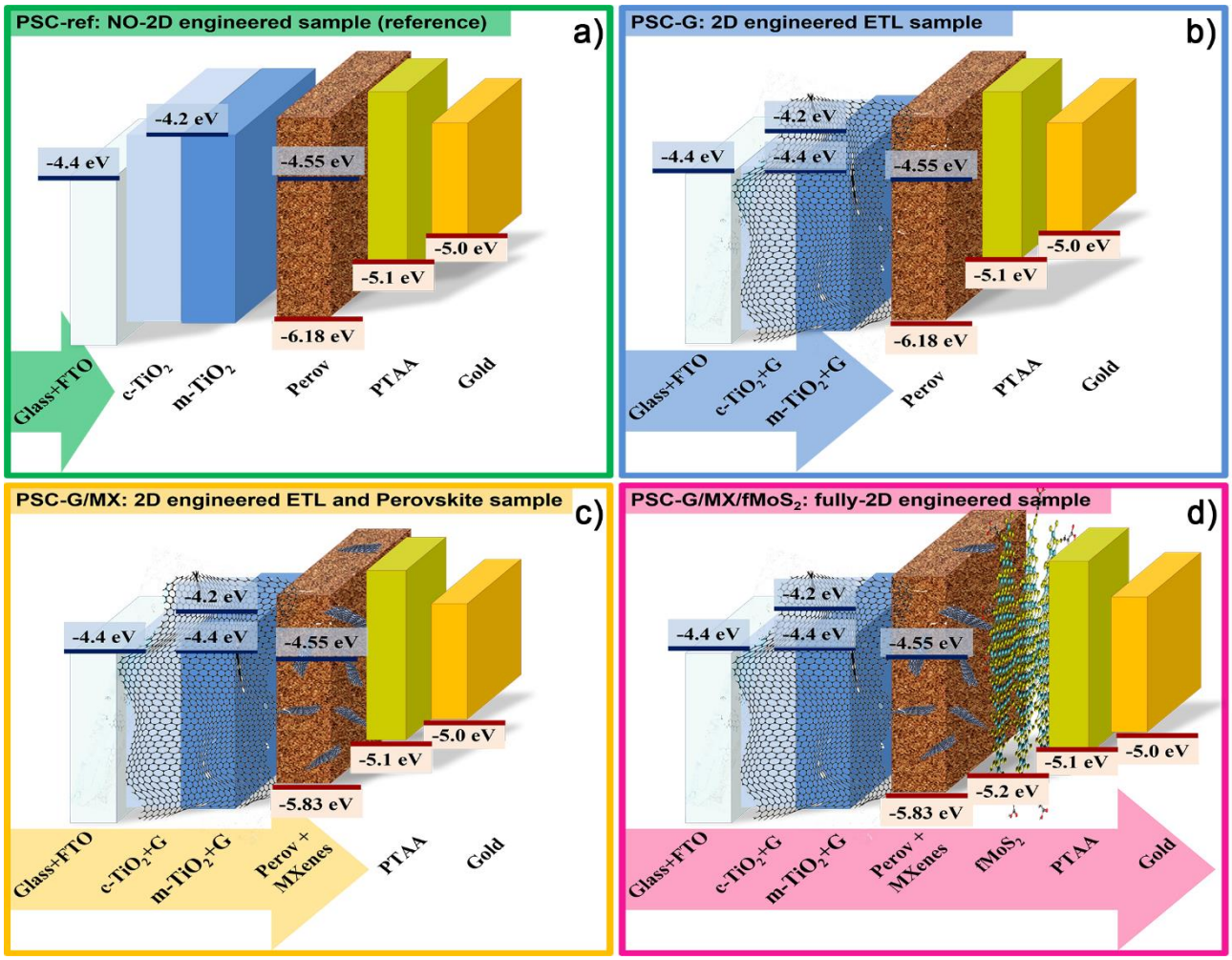

Figure 1. Structures of small-area PSCs and them relative energy band diagrams. **a) PSC-ref**: FTO/cTiO$_2$/mTiO$_2$/perovskite/PTAA/Au, the reference mesoscopic structure; **b) PSC-G**: FTO/cTiO$_2$+G/mTiO$_2$+G/perovskite/PTAA/Au with graphene modified ETL; **c) PSC-G/MX:** FTO/cTiO$_2$+G/mTiO$_2$+G/perovskite+MXenes/PTAA/Au, by doping the perovskite layer with MXenes and **d) PSC-G/MX/fMoS$_2$** FTO/cTiO$_2$+G/mTiO$_2$+G/perovskite+MXenes/fMoS$_2$/PTAA/Au, the full 2D engineering structure obtained by adding a fMoS$_2$ interlayer between perovskite and PTAA layer. The work function values for FTO, TiO$_2$ and graphene have been taken from refs.[46–48] The highest occupied molecular orbital (HOMO) and lowest

unoccupied molecular orbital (LUMO) levels for perovskite, perovskite+MXenes and PTAA have been taken from refs[23] and [49], respectively. The energy band edge positions for $fMoS_2$ have been taken from ref.[34] The band alignments are not to scale and show only the relative position of the energy levels. The depicted energies values are relative to the vacuum level.

By selecting these four different structures, it is possible to elucidate the distinct contributions stemming from the addition of each 2D material in the structure. In particular, the main effects of graphene addition into the $cTiO_2$ consists in i) an improved FF due to a decreased cell series resistance reflecting both an enhanced electron injection efficiency at the $mTiO_2$+G/perovskite interface,[12,50] and an improved electron mobility[51,52] ii) a boost in V_{OC} value, testifying a reduced impact of the charge trapping mechanism within $mTiO_2$ and/or at $cTiO_2$/$mTiO_2$/perovskite interfaces, as demonstrated by advanced electro-optical characterizations reported in the following. The improved electron dynamic, obtained by engineering the ETL with the addition of graphene in both compact and mesoscopic TiO_2 layers, reflects in an overall FF (3%) and V_{OC} (1.1%) enhancement, positively affecting the PCE that results improved up to 19.47%, with an average increase of 4%.

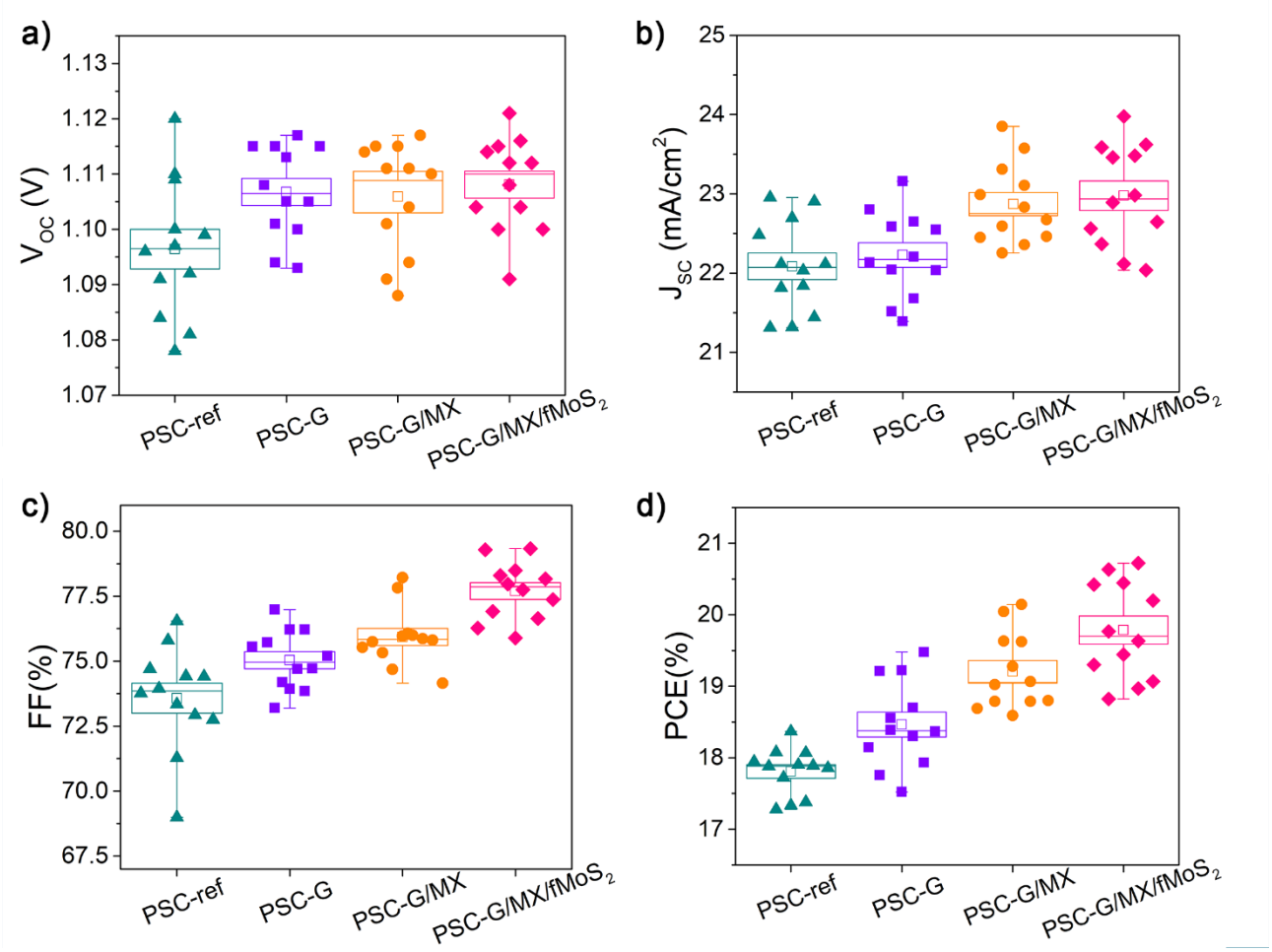

Figure 2: Photovoltaic parameters for the four investigated PSCs evaluated by 1 SUN current–voltage (I–V) characteristics: (a) open-circuit voltage V_{OC}, (b) short-circuit current density J_{SC}, (c) fill factor FF and (d) power conversion efficiency PCE. The parameters statistics were acquired over 12 PSCs for each architecture.

The addition of $Ti_3C_2T_x$ MXene (see ref.[23] for details about the MXene synthesis and characterization) to the perovskite absorber produces as main effect an increase of the J_{SC} (**Fig. 2b**). This effect was expected considering the role of $Ti_3C_2T_x$ doping of perovskite absorber that results in an enhancement of charge transfer and in a reduction of interface losses at perovskite/charge transporting layers (CTLs) interfaces leading to an enhanced J_{SC} (+3%) and FF (+1%) with respect

to the PSC-G. Indeed, the MXenes addition induces a significant reduction of the perovskite WF,[23] by further improving the band alignment at $mTiO_2$+G/perovskite interface (see **Fig.1**).
The final IE strategy was performed by inserting an additional buffer layer of $fMoS_2$ between the perovskite layer and the HTL with the idea to limit the undesirable charge recombination of electrons and holes usually at the perovskite/HTL interface. The insertion of this 2D interlayer, in addition to the graphene in the ETL and to MXenes into the perovskite, results in a drastic increase of the FF (+2.8% with respect to the PSC-G/MX) as further investigated by advanced electro-optical characterization reported in the following.
For this 2D optimized PSC we obtain a champion device showing PCE value up to 20.72%, FF = 77.75%, V_{OC} =10.06 V, and J_{SC}=23.97 mA/cm^2 (see **Fig. 3a**), due to a properly electronic energy band alignment, a suitable charge carrier mobility in ETL and HTL, but also to an effective charge extraction from the perovskite layer. Thus, the synergic use of different 2D materials into PSC structures allowed to achieve a relative PCE improvement higher than +13.2% with respect to reference champion devices. Notably PSC-G/MXenes/$fMoS_2$ device exhibits stable performance under prolonged 1 SUN irradiation at maximum power point (MPP), as reported in **Fig. 3b** (see **Fig. SI 1a,b** for the analogues characterizations in the case of PSC-ref structure).

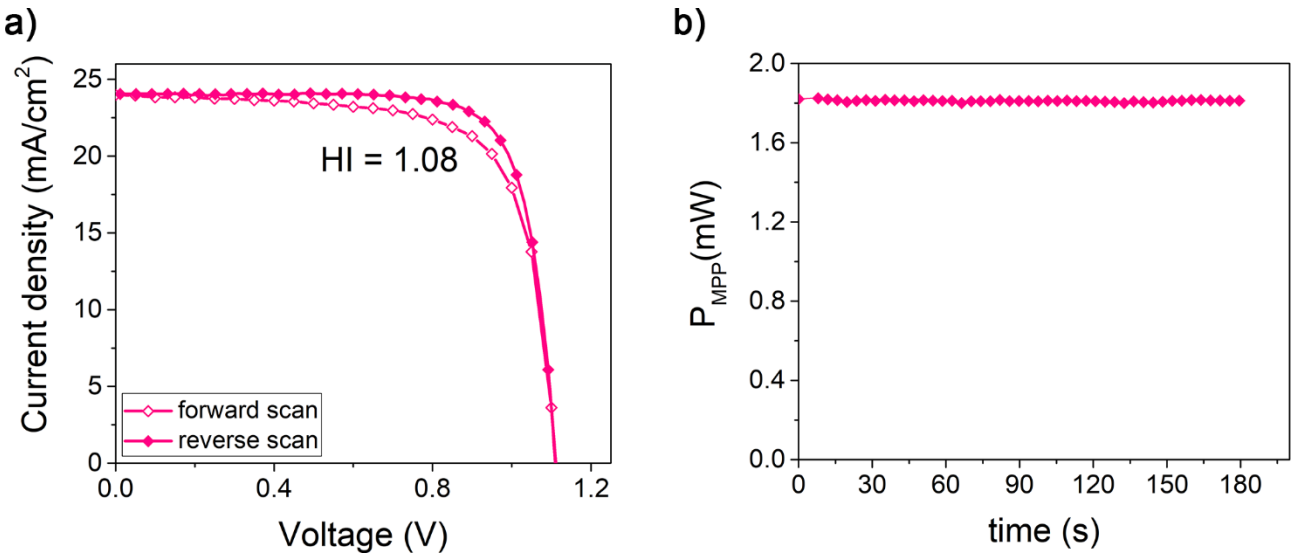

Figure 3:a) Current Density-Voltage (J_{SC}-V) forward (pink empty diamonds) and reverse (pink full diamonds) scan obtained in the case of best efficient device with optimized 2D IE (PSC-G/MXenes/$fMoS_2$). b) Maximum Power Point (MPP) tracking for the same cell structure (PSC-G/MXenes/$fMoS_2$).

With the aim to elucidate the relevant role of 2D material engineering strategy in mesoscopic PSCs, the External Quantum Efficiency (EQE) was measured for each device structure. In particular, the photocurrent extracted in short circuit condition is the result of three main processes: light harvesting from the absorber, charge transfer from the absorber to the CTLs and the charge collection at the electrodes. As evident from **Fig. 4a**, the fully 2D material engineered PSC shows a significant EQE value increase over the whole spectrum with respect to the other cell typologies. As first investigation, TAUC plot and photoluminescence (PL) emission spectra were acquired for both pristine and MXene-doped perovskite films deposited on glass (see **Fig. SI 2a** and **b**). Despite MXenes are not able to increase the light harvesting properties of perovskite absorber (as showed in **Fig. SI 2a**) their insertion into the perovskite absorber induces a not-negligible boost of radiative recombination. This is a clear indication of an improved perovskite crystal quality, that induces a reduction of trapping/de-trapping phenomena mediated by deep trap states (or grain boundaries),[53] eventually accelerating the charge dynamics within the absorber.[54] In addition, the slight blue shift of the PL peak recorded for MXenes-doped perovskite film could suggest a

reduced formation of ionic domains due to the halide segregation during the perovskite film deposition. Moreover, transient photocurrent (TPC) measurements were performed over complete devices and reported in **Fig. 4b**. In particular, the faster is the TPC decay profiles the faster is the free charge dynamics within the entire devices, indicating improved charge injection through the device interfaces and faster charge transport among the transporting layers.[55] Remarkably, the fastest TPC decay was obtained in PSC-G/MX/fMoS_2, testifying faster charge transit time and eventually faster charge extraction at the electrodes when 2D materials are suitably inserted within the PSC structure. Indeed, faster current decay in the case of PSC-G/MX/fMoS_2 suggests improved charge extraction at the CE with respect to PSC-G/MX,[56] once fMoS_2 is inserted as interlayer at perovskite+MXenes/PTAA interface. The same occurs even when graphene is added to the device ETL with respect to reference devices (see curves for PSC-ref and PSC-G in **Fig. 4b**), confirming the role of graphene to improve the negative charge collection up at the PE. In addition, transient photovoltage (TPV) measurements were performed to get further information about the charge lifetime in the proposed device structures (as reported in **Fig. 4c**).[57] In a TPV experiment, the solar cell is kept at open-circuit voltage under bias-illumination. Then an additional small laser pulse (or LED pulse) is applied to the device to create some additional charge that decays exponentially thereafter. Since no current is flowing within the device, the generated charges expire through several recombination channel. The higher is the trapping efficiency of the trap state, the lower is the charge carrier lifetime. Notably, PSC-G/MX/fMoS_2 and PSC-G/MX configurations showed the highest recombination life-times underlining a reduced impact of trap recombination upon the charge dynamics,[58] once the perovskite is doped with MXenes. Moreover, the higher charge lifetime extracted in the case of PSC-G/MX/fMoS_2 with respect to PSC-G/MX (see **Fig. 4c**) suggest a trap state passivation at perovskite/HTM interface[59] mediated by the addition of fMoS_2 interlayer.[34] As further investigation, V_{OC} trend vs light incident power (P_{inc}) was recorded and reported in **Fig. 4d**. In particular, at low irradiance level (P_{inc} < 0.2 SUN) the slope of the V_{OC} vs log(P_{inc}) plot is related to the electron quasi-Fermi level, which is determined by the charge accumulation and density of states in the ETL (i.e., cTiO_2+G/mTiO_2+G).[60] Notably, devices employing graphene-based ETL showed increased V_{OC}(P_{inc}) slope with respect to PSC-ref employing pristine ETL, by testifying a reduction in the charge trapping rate within mTiO_2 or at cTiO_2/mTiO_2 and mTiO_2/perovskite interface. For larger P_{inc} (>0.2 SUN), the energy states of the ETL are fully filled, and the charge generation and recombination rates within the device determine the slope of the V_{OC} vs log(P_{inc}). Thus, the lower V_{OC} (P_{inc}) slope in the case of PSC-G/MX and PSC-G/MX/fMoS_2 suggests a lower impact of trap states at perovskite/CTL interfaces over the carrier dynamics, once the MXene addition within the perovskite absorber. Finally, when fMoS_2 interlayer is embedded in the structure, the improved energy band alignment between MXene-doped perovskite absorber and PTAA reflects in a higher α coefficient for J_{SC}(P_{inc}) plot, once fitted with a power law $J_{SC} \propto I^{\alpha}$ (see **Fig. SI 3**). Indeed, despite both investigated device structures PSC-G/MX/fMoS_2 and PSC-G/MX showed α values very close to 1, evidencing no space-charge limited behaviour,[61] a slightly higher α value is obtained for PSC-G/MX/fMoS_2, evidencing an improved charge transfer[62] at perovskite+MXenes/PTAA interface when fMoS_2 interlayer is introduced.

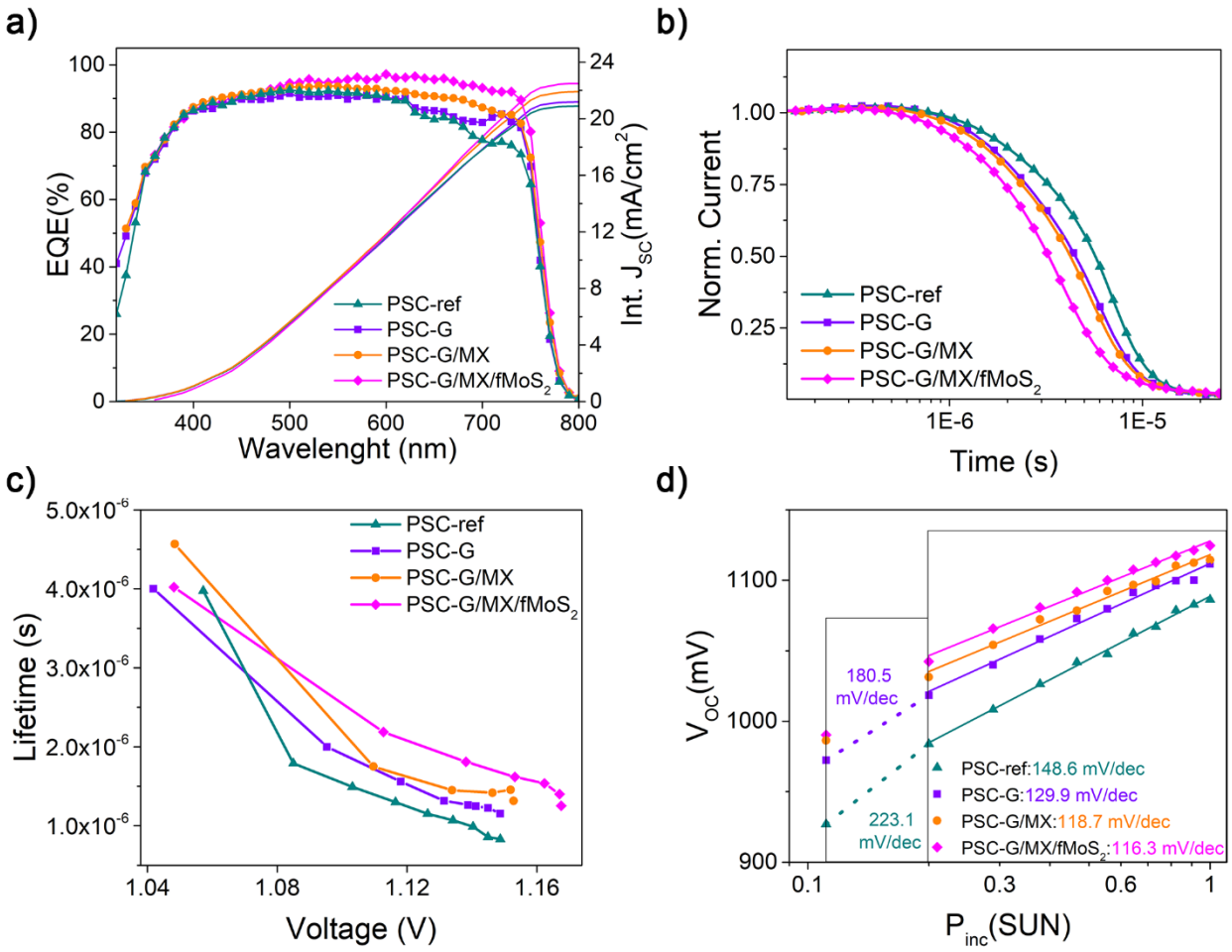

Figure 4: **a**) External Quantum Efficiency (EQE) spectra with the extrapolated integrated photocurrent density (Integrated J_{SC}) related to the best efficient cell for each proposed device structure. **b**) Transient photocurrent decay profiles acquired on all the investigated device structures. Faster exponential current rise after light turn-on evidences better charge dynamics. **c**) Charge carrier lifetime extracted by the small-signal TPV decay profiles and **d**) V_{OC} light intensity-dependence [$V_{OC}(P_{inc})$] of PSCs for all the investigated device typologies. Linear fitting of the curves has been performed for both P_{inc}<0.2 SUN and P_{inc}>0.2 SUN, and the respective slope values are reported on the plot or in the label, respectively.

Furthermore, since the charge trapped at the interfaces is well known to trigger degradation,[63] we can assert that the use of 2D materials reflected in a stabilization effect mainly attributable to the improved charge extraction as testified by the monotonic behavior of the MPP tracking observed in the first 180 s (**Fig. 3b**).

By following this approach, we found as a further advantage, a reduction of J-V hysteresis in the case of fully engineered PSC-G/MX/fMoS$_2$. In detail, by evaluating the hysteresis index (HI), defined as the ratio between the efficiency obtained from reverse J-V scan (varied from V=V_{OC} to V=0) and the respective forward J-V scan, a HI reduction can be observed moving from 1.19 in the case of reference sample (**Fig. SI 1a**) to 1.08 for PSC-G/MX/fMoS$_2$ **(Fig 3a)**. As further confirmation, in **Fig. SI 1b** we reported the MPP tracking for the reference cell type, where a 26% power drop-off can be observed in first 180 s. This behavior testifies a slower electron dynamic causing a faster degradation when no tailored IE is used. Indeed, even in mixed-halide and multi-cation perovskite systems, ionic segregations have been demonstrated to occur during prolonged light soaking conditions, by affecting the perovskite film optoelectronic properties and eventually carrier recombination dynamics within the device. As suggested by several studies,[64,65]

illumination leads to the formation of spatially inhomogeneous lower-energy iodide-rich sites on the perovskite film that grow in size over time.[38] This can be probed by acquiring PL emission spectra over time once the device photo-electrode (PE) is exposed to sun simulator radiation. Thus, with the aim to assess the role of 2D materials in stabilizing the chemical and optoelectronic properties of the perovskite absorber, we exposed opened PEs used in both reference and fully 2D materials engineered devices, under prolonged 1 SUN illumination, by progressively acquiring the PL spectra. The extracted PL intensity and peak position over stress time are reported in **Fig. SI 4**. The PL intensity increase over time was observed to be higher for reference sample, demonstrating the major impact of ionic domain formation over the perovskite degradation. Indeed, when this occurs in complete device, photogenerated charge carriers transfer onto these domains by recombining with high radiative efficiency.[66] This is due to a combination of a photoinduced trap reduction and a high local concentration of charges on the low-bandgap (LG) emitting sites. Already after 10 min of light treatment, the LG peak dominates the emission by inducing a red-shift of the main PL peak. This effect is more marked for reference PEs, giving the evidence of the stabilizing effect attributed to the use of 2D materials.

3.2 Large area modules

We extended the promising use of graphene and other 2D materials to large area modules as a powerful tool to mitigate the losses induced by the scaling-up of the device dimensions, by eventually reduce the efficiency gap between small area cells and scaled modules. Following the typical module architecture of thin films photovoltaics, we fabricate PSM by connecting cells in series. The interconnection scheme results in an alternation of active zones that are dedicated to the photogeneration of electric charges, and dead zones, not contributing to the PV energy conversion, dedicated to the interconnection between adjacent cells. Interconnections are defined by laser process that has been demonstrated to be an optimal choice for their manufacture[67,68] via the P1, P2, P3 patterning. Briefly, P1 step insulates the photoanodes of neighbouring cells, P2 step selectively removes the entire stack of active materials between adjacent cells, and P3 step remove the counter electro connection between the cells. By using the laser system (Nd:YVO4 UV (80 kHz)—Spectra Physics Explorer One HP 355-4) we were able to realize monolithic interconnected series modules, with different size substrate area of 11×11 cm^2 and 14.5×14.5 cm^2, as showed in **Fig. 5a** and **5c** respectively (see materials and methods section for detailed description of the PSM manufacturing). The small modules consisting in nine series connected PSCs (cell active area 9.18 cm^2) with an overall active area of 82.62 cm^2, while the larger ones exhibit a total active area of 137.16 cm^2, resulting in twelve cells (cell active area 11.44 cm^2). The same structures tested for small-area PSCs, were considered for both large area modules and named as PSM-ref, PSM-G, PSM-G/MX, and PSM-G/MX/fMoS_2, following the notation used for small area PSCs. The best I-V curves, obtained for the fully engineered typology (PSM-G/MX/fMoS_2), which combines the use of graphene in ETL, MXenes in perovskite layer and fMoS_2 as interlayer at interface between perovskite and HTL, are shown in **Fig. 5b** and **5d** for two different active areas, while in **Table 1** the related photovoltaic parameters obtained for the champion efficiencies (for both forward and reverse scan) are reported.

Table1: Photovoltaic parameters V_{OC} (V), I_{SC}(mA), FF(%), PCE(%) for the best performing PSM-G/MX/fMoS_2 modules (121 cm^2 and 210 cm^2 substrate area) extracted by the related I-V curves, acquired under 1 SUN irradiation by scanning the potential in reverse (full symbols) and forward (empty symbols) direction.

	Substrate Area (cm^2)	Aperture Area (cm^2)	Active Area (cm^2)	V_{OC} (V)	I_{SC}(mA)	FF(%)	PCE(%) [Active Area]	Scan verse

PSM-G/MX/fMoS$_2$	121	98.94	82.62	10.06	210	67.29	17.2	reverse
				9.84	214	61.43	15.6	*forward*
PSM-G/MX/fMoS$_2$	210	160.02	137.16	12.83	259	60.59	14.7	reverse
				12.49	260	55.14	13.1	*forward*

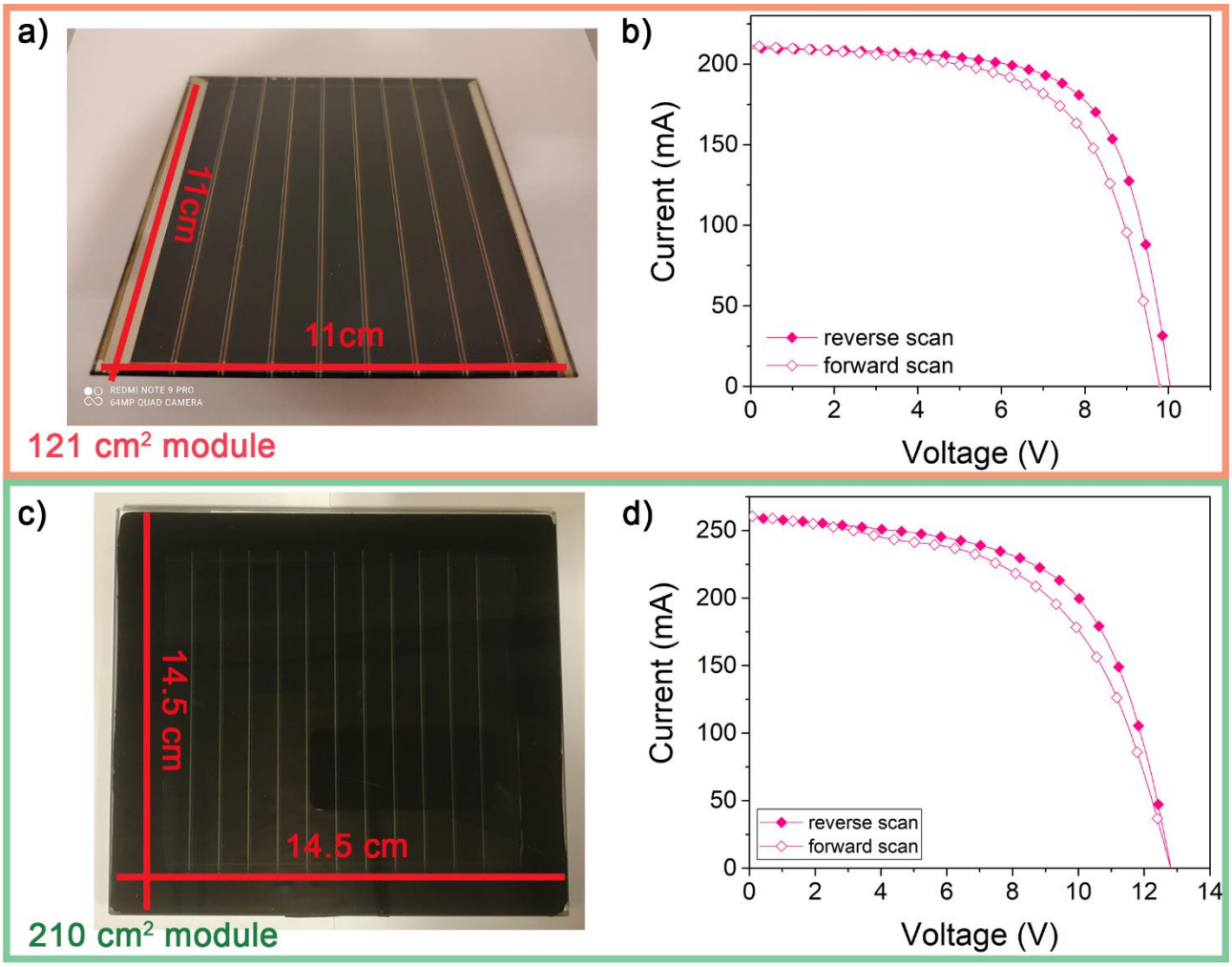

Figure 5: Photograph of a representative large-area PSM-G/MX/fMoS$_2$ a) 121 cm^2 and c) 210 cm^2 substrate area. I–V characteristics of champions PSMs acquired under 1 SUN illumination with an active area of b) 82.62 cm^2 and d) 137.16 cm^2.

As already discussed in the case of small area cells, we can also observe for large area devices, the same trends of photovoltaic parameter statistics. In fact, as showed in **Fig.6 b** and **d**, the module average electrical parameters were improved (see also **Fig. SI 5**) moving from PSM-ref to PSM-G/MX/fMoS$_2$, by confirming the crucial role of IE in retaining high PCE values when scaling the active area dimension up. In particular, we observed a gain of 10.4% (11.7%) and 18.2% (22.5%) in PCE average (champion device PCE) values in the case of PSM-G/MX/fMoS$_2$ with respect to the reference PSM-ref for 121cm^2 and 210 cm^2 modules respectively, confirming the effectiveness of 2D material engineering strategy when device active area is enlarged. Moreover, for the PSM-G/MX/fMoS$_2$ typology, the V_{OC} reaches average values of 10.06 V (12.68 V) for 121 cm^2 (and 210 cm^2) substrate area, indicating that each separate sub-cell delivers an average V_{OC} as high as 1.12 V (1.06 V), in agreement with the one measured on small-area PSCs (1.10 V). This trend could corroborate there are no recombination mechanisms, linked to the enlargement of active area device, that the 2D materials cannot counterbalance.

The stabilized power outputs at MPP (P_{MPP}) for both 121 and 210 cm^2 PSM-G/MX/fMoS_2 are reported in **Fig. SI 6**, confirming the stabilization effect operated by the 2D material-based IE approach, as already observed in the case of small area devices.

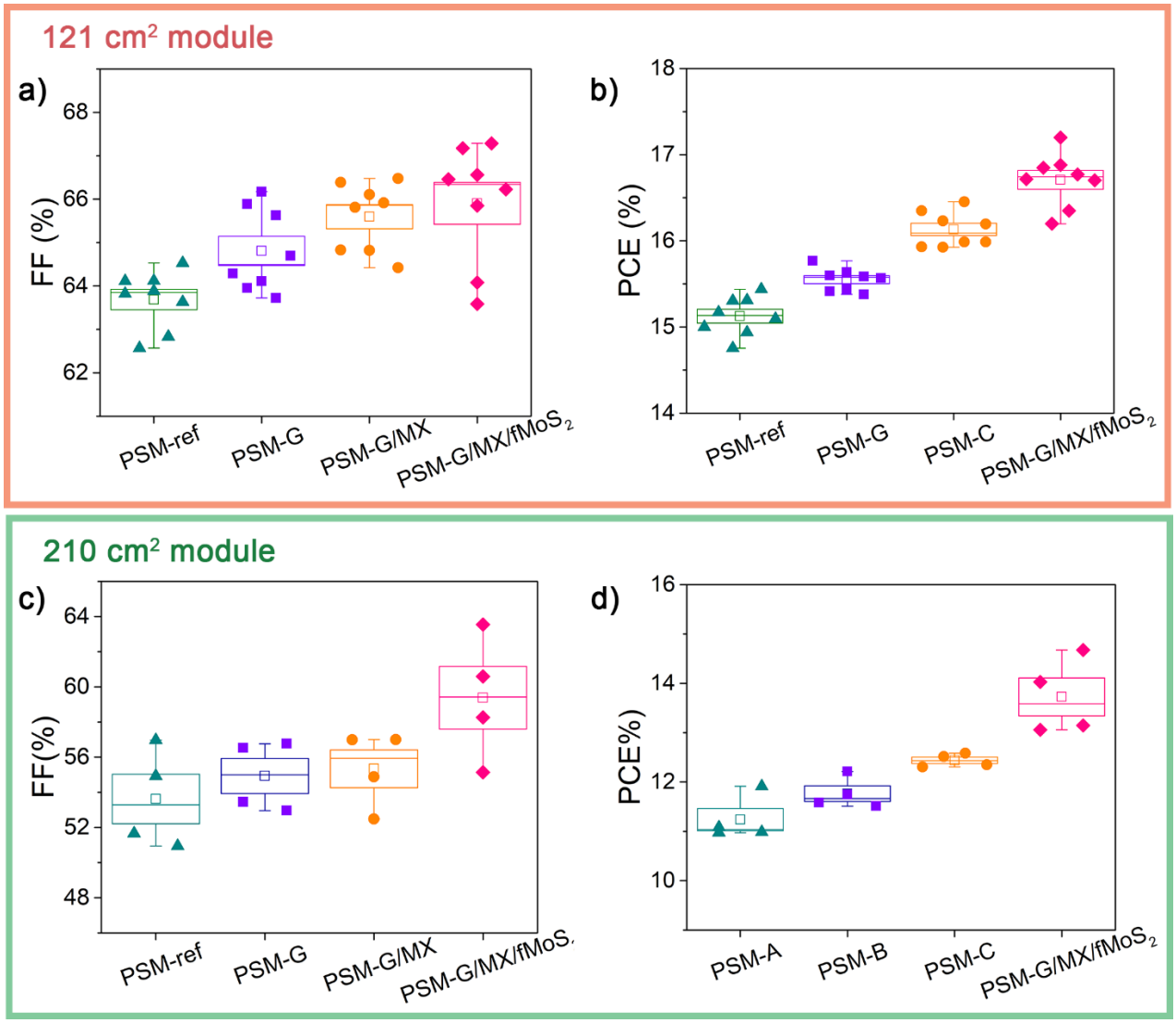

Figure 6: Photovoltaic parameters for the four investigated PSMs evaluated by 1 SUN current–voltage (I–V) characteristics for both dimensions 121 cm^2 (a) FF, (b) PCE, and 210 cm^2 (c) FF and (d) PCE. The statistics were measured on 8 PSMs (121 cm^2) and on 4 PSMs (210 cm^2) respectively for each tested structure.

Finally, with the aim to assess the role of 2D materials also on stability of PSMs, we performed a prolonged thermal stress lasting 1056 hours at 85°C on 121cm^2 PSMs (reference and fully 2D engineered) by monitoring photovoltaic parameters on encapsuled devices, as reported in **Fig. 7**. The device encapsulation consists in glass-glass sealing with Three Bond glue as edge sealer. To compare the effect of temperature stress on photovoltaic parameters for different module structures, we normalized the electrical performance values extracted by the I-V characteristics to the respective initial values (t = 0 h).

Regarding the effect of thermal stress on PSMs during the first 24 hours, it can be observed a similar drop of the electrical performance for both typologies, reflecting in a reduction of P_{MAX} (**Fig. 7d**), mainly related to an abrupt decrease of both V_{OC} (**Fig. 7a**), and I_{SC} (**Fig. 7b**). This effect can be attributed to an initial chemical instability of the perovskite material as a function of the temperature when ion's migration occurred by leading vacancies and bromine and iodide

segregations in the perovskite crystal structure. At the same time, the laser process triggers the same degradation phenomenon for both types of PSM. After this initial drop, the combined use of 2D materials in the module structure results in a considerably improved stability with respect to the reference module. In fact, during the thermal stress, functional properties of each layer may degrade over time, even when carefully protected.[69] The active layer, the HTL and ETL, and each of their interfaces may experience undesirable changes in microstructure,[70] chemistry,[71] and thereby functional properties, by losing 80% of the initial P_{MAX} in less than 90 hours (see reference device PCE trend in **Fig. 7d**).

On the contrary, using a fully combined 2D engineering material strategy can improve the device durability by retaining 80% of initial P_{MAX} value for more than 530 hours. More in detail, the addition of graphene flakes into $mTiO_2$ scaffold produces a twofold advantage. From one side, the perovskite crystals embedded in $mTiO_2$+G exhibits trap state density one order of magnitude lower with respect to that obtained in the case of pristine $mTiO_2$ layer.[12] From the other side, during cell aging, a stabilization of carrier temperature occurred due to the improved stability of perovskite crystals embedded in $mTiO_2$+G.[15,72] Furthermore, the locally-inhomogeneous light-induced back-conversion of perovskite layer into PbI_x and PbO_x species can be slowed-down by the presence of graphene in the $mTiO_2$. Consequently, the amount of free iodine species that can diffuse across the interfaces is reduced by hampering the induced chemical modifications at the gold electrode (Au-I bonding) and the mesoscopic TiO_2 (Ti-I bonding) interfaces. Thus, the gold diffusion across the entire device structure is highly inhibited.[13] In the same way, the presence of $fMoS_2$ buffer layer can mitigate the localized gold and iodine diffusion within PSMs, by concurring to the slowing of device aging and consequent decrease in performance during the prolonged thermal stress.[34]

In this context, also MXenes can take part to the stabilization process of the device structure due to the demonstrated improved charge extraction, since trapped charges at the interfaces are well known to trigger degradation.[23]

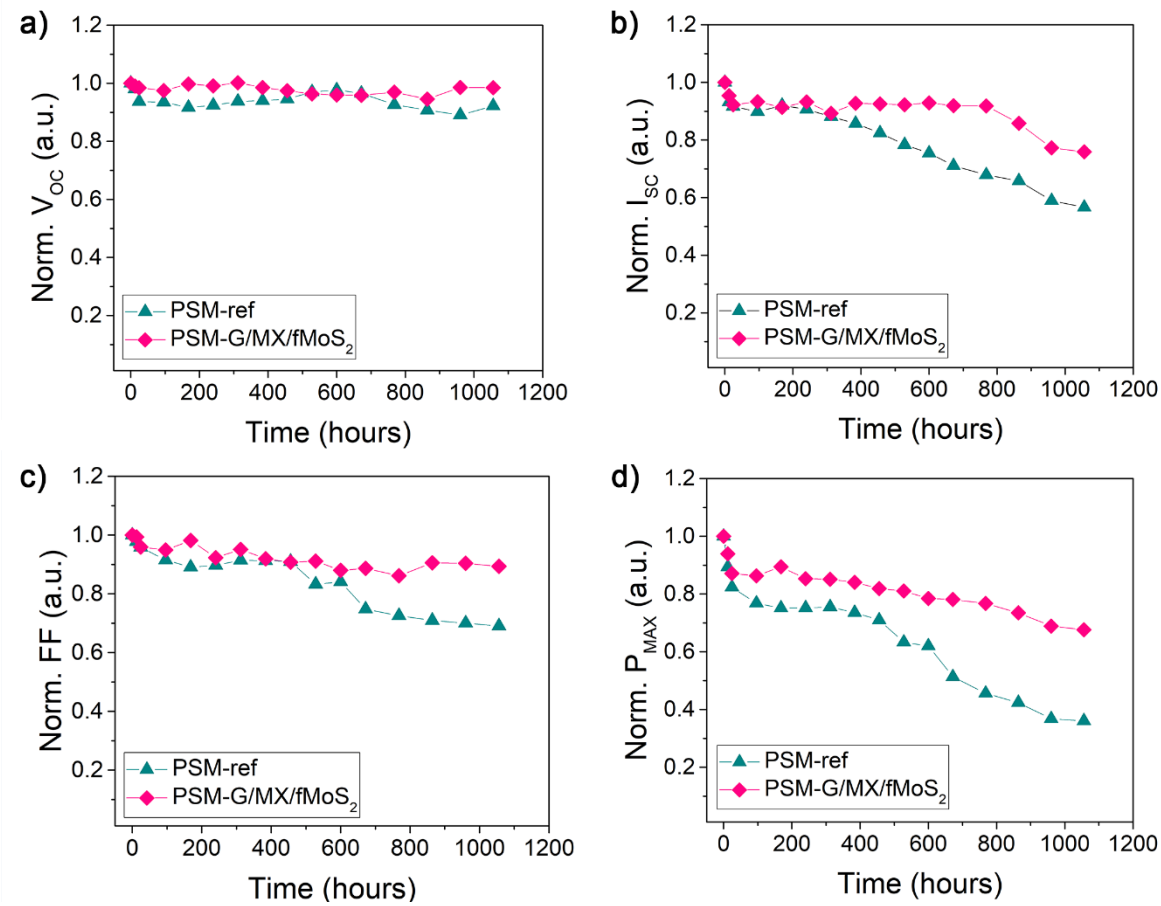

Figure 7: The effect of prolonged (1056 hours) thermal stress (85°C) on 121 cm^2 PSMs (reference vs fully 2D engineered) with respect to their photovoltaic parameters a) V_{OC}, b) I_{SC}, c) FF and d) P_{MAX} normalized to the initial values.

4. Conclusions

In this work we exploited the vast library of two-dimensional materials to design an interface engineering (IE) strategy, improving the performances of perovskite solar cells and large area modules. In particular, we exploited specific 2D materials on different layer of the cells. Based on developed know-how we chose graphene to master the properties of compact and mesoscopic TiO_2, $Ti_3C_2T_x$ MXenes to tune the WF of the perovskite absorber and $fMoS_2$ to reduce charge recombination at the perovskite/HTL interface. In particular, the as-realized mesoscopic structure: FTO/$cTiO_2$+G/$mTiO_2$+G/perovskite+MXenes/$fMoS_2$/PTAA/AU was firstly tested and optimized on small area cells (active area 0.09 cm^2) by reaching photo conversion efficiency (PCE) exceeding 20%. The same 2D material-engineered structure was used on 11×11 cm^2 large area modules (active area 82.62 cm^2), showing top PCE value of 17.2%, while an impressive PCE above 14.7% was achieved for 14.5×14.5 cm^2 (active area 137.16 cm^2) modules. In fact, the here proposed 2D material IE approach can be easily scaled-up to large area modules, since the 2D material dopants (graphene and MXenes) involve only the precursor solutions without impacting on the deposition methods. On the other hand, the deposition of $fMoS_2$ interlayer can be done by the scalable spray coating technique.[25]

The proposed full 2D material engineered PSC structure demonstrated an enhancement of charge extraction at perovskite/CTL interfaces and a reduction of non-radiative charge losses due to a proper energy offset between perovskite absorber and CTLs, leading to higher J_{SC} and larger FF.

Hence, an optimized energy level alignment is of utmost importance for getting ideal open-circuit voltage (V_{OC}), by minimizing the carrier recombination losses and reducing the hysteretic behavior of PSC.
Finally, despite statistical analysis on large area devices is seldom reported in literature, here the effectiveness of 2D material-based engineering strategy in enlarging the module active area by preventing the typical PCE drop-off is demonstrated over a large PSMs number. The presented advances can reduce the gap from lab-scale to marketable devices, a step further toward the industrial deployment of this technology.

ACKNOLEDGEMENTS
We gratefully acknowledge the funding from the European Union's Horizon 2020 research and innovation programme under grant agreement No SGA 881603 GrapheneCore3. ADC Acknowledge the financial support of MISSION INNOVATION project of Italian MISE. We thank S. Bellani for fruitful discussion.

Author Contributions
SP, AA, and ADC conceived the work. SP, AA, performed the experiment on small and large area devices, the electro-optical characterizations, and the stress test while SR performed the optimization of laser processing for module production. HP, LN, and FB provided 2D materials. The manuscript was written through contributions of all authors. All authors have given approval to the final version of the manuscript.

References

[1] https://www.nrel.gov/pv/assets/images/efficiency-chart.png (accessed on 27 December 2020), (n.d.).

[2] M. Grätzel, The light and shade of perovskite solar cells, Nat. Mater. 13 (2014) 838–842. doi:10.1038/nmat4065.

[3] H.J. Snaith, A. Abate, J.M. Ball, G.E. Eperon, T. Leijtens, N.K. Noel, et al., Anomalous Hysteresis in Perovskite Solar Cells, J. Phys. Chem. Lett. 5 (2014) 1511−1515. doi:10.1021/jz500113x.

[4] B. Conings, J. Drijkoningen, N. Gauquelin, A. Babayigit, J. D'Haen, L. D'Olieslaeger, et al., Intrinsic Thermal Instability of Methylammonium Lead Trihalide Perovskite, Adv. Energy Mater. 5 (2015) 1500477. doi:10.1002/aenm.201500477.

[5] T.A. Berhe, W.-N. Su, C.-H. Chen, C.-J. Pan, J.-H. Cheng, H.-M. Chen, et al., Organometal halide perovskite solar cells: degradation and stability, Energy Environ. Sci. 9 (2016) 323–356. doi:10.1039/C5EE02733K.

[6] F. Giustino, H.J. Snaith, Toward Lead-Free Perovskite Solar Cells, ACS Energy Lett. 1 (2016) 1233–1240. doi:10.1021/acsenergylett.6b00499.

[7] G. Niu, X. Guo, L. Wang, Review of Recent Progress in Chemical Stability of Perovskite Solar Cells, J. Mater. Chem. A. 2 (2015) Advance. doi:10.1039/C4TA04994B.

[8] Y. Wang, Z. Zhang, M. Tao, Y. Lan, M. Li, Y. Tian, et al., Interfacial modification towards highly efficient and stable perovskite solar cells, Nanoscale. 12 (2020) 18563–18575. doi:10.1039/d0nr05136e.

[9] N. Ahn, K. Kwak, M.S. Jang, H. Yoon, B.Y. Lee, J. Lee, et al., Trapped charge-driven degradation of perovskite solar cells, Nat. Commun. 8 (2016) 1–9. doi:10.1038/ncomms13422.

[10] C.M. Wolff, P. Caprioglio, M. Stolterfoht, D. Neher, Nonradiative Recombination in Perovskite Solar

Cells: The Role of Interfaces, Adv. Mater. 31 (2019) 1902762. doi:10.1002/adma.201902762.

[11] A. Di Carlo, A. Agresti, F. Brunetti, S. Pescetelli, Two-dimensional materials in perovskite solar cells, J. Phys. Energy. 2 (2020) 031003. doi:10.1088/2515-7655/ab9eab.

[12] F. Biccari, F. Gabelloni, E. Burzi, M. Gurioli, S. Pescetelli, A. Agresti, et al., Graphene-Based Electron Transport Layers in Perovskite Solar Cells: A Step-Up for an Efficient Carrier Collection, Adv. Energy Mater. 1701349 (2017) 1–8. doi:10.1002/aenm.201701349.

[13] Y. Busby, A. Agresti, S. Pescetelli, A. Di Carlo, C. Noel, J.-J. Pireaux, et al., Aging effects in interface-engineered perovskite solar cells with 2D nanomaterials: A depth profile analysis, Mater. Today Energy. 9 (2018) 1–10. doi:10.1016/j.mtener.2018.04.005.

[14] S. Pescetelli, A. Agresti, A. Di Carlo, F. Bonaccorso, Y. Busby, Graphene and Related 2D Materials: A Winning Strategy for Enhanced Efficiency and Stability in Perovskite Photovoltaics, IEEE 4th Int. Forum Res. Technol. Soc. Ind. RTSI 2018 - Proc. (2018) 1–4. doi:10.1109/RTSI.2018.8548350.

[15] P. O'Keeffe, D. Catone, A. Paladini, F. Toschi, S. Turchini, L. Avaldi, et al., Graphene-induced improvements of perovskite solar cell stability: effects on hot-carriers., Nano Lett. 19 (2019) 684–691. doi:10.1021/acs.nanolett.8b03685.

[16] A.S.R. Bati, M. Batmunkh, J.G. Shapter, Emerging 2D Layered Materials for Perovskite Solar Cells, Adv. Energy Mater. 1902253 (2019) 1–21. doi:10.1002/aenm.201902253.

[17] F. Bonaccorso, L. Colombo, G. Yu, M. Stoller, V. Tozzini, A.C. Ferrari, et al., 2D materials. Graphene, related two-dimensional crystals, and hybrid systems for energy conversion and storage, Science (80-.). 347 (2015) 1246501. doi:10.1126/science.1246501.

[18] R. Swartwout, M.T. Hoerantner, V. Bulović, Scalable Deposition Methods for Large-area Production of Perovskite Thin Films, Energy Environ. Mater. 2 (2019) 119–145. doi:10.1002/eem2.12043.

[19] B. Taheri, N.Y. Nia, A. Agresti, S. Pescetelli, C. Ciceroni, A.E. Del Rio Castillo, et al., Graphene-engineered automated sprayed mesoscopic structure for perovskite device scaling-up., 2D Mater. 5 (2018) 045034. doi:10.1088/2053-1583/aad983.

[20] S. Pescetelli, A. Agresti, S. Razza, L.A. Castriotta, A. Di Carlo, Large area perovskite solar modules with improved efficiency and stability, 2019 Int. Symp. Adv. Electr. Commun. Technol. (2019) 1–5.

[21] B. Wang, J. Iocozzia, M. Zhang, M. Ye, S. Yan, H. Jin, et al., The charge carrier dynamics, efficiency and stability of two-dimensional material-based perovskite solar cells, Chem. Soc. Rev. 48 (2019) 4854–4891. doi:10.1039/c9cs00254e.

[22] D. Saranin, S. Pescetelli, A. Pazniak, D. Rossi, A. Liedl, A. Yakusheva, et al., Transition metal carbides (MXenes) for efficient NiO-based inverted perovskite solar cells, Nano Energy. 82 (2021) 105771. doi:10.1016/j.nanoen.2021.105771.

[23] A. Agresti, A. Pazniak, S. Pescetelli, A. Di Vito, D. Rossi, A. Pecchia, et al., Titanium-carbide MXenes for work function and interface engineering in perovskite solar cells, Nat. Mater. 18 (2019) 1228–1234. doi:10.1038/s41563-019-0478-1.

[24] A. Agresti, S. Pescetelli, B. Taheri, A.E. Del Rio Castillo, L. Cinà, F. Bonaccorso, et al., Graphene-Perovskite Solar Cells Exceed 18 % Efficiency: A Stability Study, ChemSusChem. 9 (2016) 2609–2619. doi:10.1002/cssc.201600942.

[25] L. Najafi, B. Taheri, B. Martín-García, S. Bellani, D. Di Girolamo, A. Agresti, et al., MoS2 Quantum Dot/Graphene Hybrids for Advanced Interface Engineering of a $CH_3NH_3PbI_3$ Perovskite Solar Cell with an Efficiency of over 20%, ACS Nano. 12 (2018) 10736–10754. doi:10.1021/acsnano.8b05514.

[26] R. Verduci, A. Agresti, V. Romano, G. D'angelo, Interface engineering for perovskite solar cells based

on 2d-materials: A physics point of view, Materials (Basel). 14 (2021) 1–17. doi:10.3390/ma14195843.

[27] A. Nourbakhsh, L. Yu, Y. Lin, M. Hempel, S. R.-J., D. Englund, et al., Beyond-CMOS Technologies for Next Generation Computer Design, in: Springer, 2019: pp. 43–84.

[28] S. Kang, D. Lee, J. Kim, A. Capasso, H.S. Kang, J. Park, 2D semiconducting materials for electronic and optoelectronic applications: potential and challenge, 2D Mater. 7 (2020) 022003. doi:10.1088/2053-1583/ab6267.

[29] C. Han, Y. Zhang, P. Gao, S. Chen, X. Liu, Y. Mi, et al., High-Yield Production of MoS_2 and WS_2 Quantum Sheets from Their Bulk Materials, Nano Lett. 17 (2017) 7767–7772. doi:10.1021/acs.nanolett.7b03968.

[30] D. Konios, G. Kakavelakis, C. Petridis, K. Savva, E. Stratakis, E. Kymakis, Highly efficient organic photovoltaic devices utilizing work-function tuned graphene oxide derivatives as the anode and cathode charge extraction layers, J. Mater. Chem. A. 4 (2016) 1612–1623. doi:10.1039/C5TA09712F.

[31] P. Snapp, J.M. Kim, C. Cho, J. Leem, Interaction of 2D materials with liquids : wettability , electrochemical properties , friction , and emerging directions, NPG Asia Mater. 12:22 (2020) 1–16. doi:10.1038/s41427-020-0203-1.

[32] S. Yano, K. Sato, J. Suzuki, H. Imai, Y. Oaki, Amorphous 2D materials containing a conjugated-polymer network, Commun. Chem. 2:97 (2019) 1–9. doi:10.1038/s42004-019-0201-9.

[33] W.H. Lee, Y.D. Park, Tuning Electrical Properties of 2D Materials by Self-Assembled Monolayers, Adv. Mater. (2017) 1700316. doi:10.1002/admi.201700316.

[34] A. Agresti, S. Pescetelli, A.L. Palma, B. Martin-Garcia, L. Najafi, S. Bellani, et al., Two-dimensional (2D) Material Interface Engineering for Efficient Perovskite Large-area Modules., ACS Energy Lett. 4 (2019) 1862–1871. doi:10.1021/acsenergylett.9b01151.

[35] A. Capasso, F. Matteocci, L. Najafi, M. Prato, J. Buha, L. Cinà, et al., MoS_2 flakes as active buffer layer for stable perovskite solar cells, Adv. Energy Mater. 6 (2016) 1600920. doi:10.1002/acnm.201600920.

[36] X. Chen, N.C. Berner, C. Backes, G.S. Duesberg, A.R. McDonald, Functionalization of Two-Dimensional MoS_2: On the Reaction between MoS_2 and Organic Thiols, Angew. Chem. Int. Ed. 55 (2016) 5803–5808. doi:10.1002/anie.201510219.

[37] A. Förster, S. Gemming, G. Seifert, D. Tománek, Chemical and Electronic Repair Mechanism of Defects in MoS2 Monolayers, ACS Nano. 11 (2017) 9989–9996. doi:10.1021/acsnano.7b04162.

[38] R. Larciprete, A. Agresti, S. Pescetelli, H. Pazniak, A. Liedl, P. Lacovig, et al., Moixed cation halide perovskite under environmental and physical stress, Materials (Basel). 14 (2021) 3954 (1–20).

[39] Z. Guo, L. Gao, Z. Xu, S. Teo, C. Zhang, Y. Kamata, et al., High Electrical Conductivity 2D MXene Serves as Additive of Perovskite for Efficient Solar Cells, Small. 1802738 (2018) 1–8. doi:10.1002/smll.201802738.

[40] L. Yang, Y. Dall'Agnese, K. Hantanasirisakul, C.E. Shuck, K. Maleski, M. Alhabeb, et al., SnO2-Ti3C2 MXene electron transport layers for perovskite solar cells, J. Mater. Chem. A. 7 (2019) 5635–5642. doi:10.1039/C8TA12140K.

[41] P. You, G. Tang, F. Yan, Two-dimensional materials in perovskite solar cells, Mater. Today Energy. 11 (2019) 128–158. doi:10.1016/j.mtener.2018.11.006.

[42] A. Agresti, S. Pescetelli, A.L. Palma, A.E.D.R. Castillo, D. Konios, G. Kakavelakis, et al., Graphene interface engineering for perovskite solar module: 12.6% Power Conversion Efficiency over 50 cm^2

Active Area, ACS Energy Lett. 2 (2017) 279–287. doi:10.1021/acsenergylett.6b00672.

[43] A. Agresti, S. Pescetelli, E. Gatto, M. Venanzi, A. Di Carlo, Polyiodides formation in solvent based Dye Sensitized Solar Cells under reverse bias stress, J. Power Sources. 287 (2015) 87–95. doi:10.1016/j.jpowsour.2015.04.038.

[44] A. Agresti, L. Cinà, S. Pescetelli, B. Taheri, A. Di Carlo, Stability of dye-sensitized solar cell under reverse bias condition: Resonance Raman spectroscopy combined with spectrally resolved analysis by transmittance and efficiency mapping, Vib. Spectrosc. 84 (2016) 106–117. doi:10.1016/j.vibspec.2016.03.008.

[45] A. Agresti, S. Pescetelli, A. Quatela, S. Mastroianni, T.M. Brown, A. Reale, et al., Micro-Raman analysis of reverse bias stressed dye-sensitized solar cells, RSC Adv. 4 (2014) 12366. doi:10.1039/c3ra47797e.

[46] M. Graetzel, Photoelectrochemical cells, Nature. 414 (2001) 338–344.

[47] I. Chung, B. Lee, J. He, R.P.H. Chang, M.G. Kanatzidis, All-solid-state dye-sensitized solar cells with high efficiency, Nature. 485 (2012) 486–490. doi:10.1038/nature11067.

[48] K.C. Kwon, K.S. Choi, S.Y. Kim, Increased work function in few-layer graphene sheets via metal chloride Doping, Adv. Funct. Mater. 22 (2012) 4724–4731. doi:10.1002/adfm.201200997.

[49] C.-C. Chueh, C.-Z. Li, A.K.-Y. Jen, Recent progress and perspective in solution-processed Interfacial materials for efficient and stable polymer and organometal perovskite solar cells, Energy Environ. Sci. 8 (2015) 1160–1189.

[50] A. Agresti, S. Pescetelli, L. Najafi, A.E.D.R. Castillo, Y. Busby, A. Di Carlo, Graphene and related 2D materials for high efficient and stable perovskite solar cells, in: Proc. 17th IEEE Int. Conf. Nanotechnol. Pittsburgh, 2017: pp. 145–150.

[51] G. Volonakis, F. Giustino, Ferroelectric Graphene-Perovskite Interfaces, J. Phys. Chem. Lett. 6 (2015) 2496–2502. doi:10.1021/acs.jpclett.5b01099.

[52] Y.T. Liang, B.K. Vijayan, K.A. Gray, M.C. Hersam, Minimizing graphene defects enhances titania nanocomposite-based photocatalytic reduction of CO2 for improved solar fuel production, Nano Lett. 11 (2011) 2865–2870. doi:10.1021/nl2012906.

[53] A.Y. Polyakov, N.B. Smirnov, I. V. Shchemerov, D.S. Saranin, T.S. Le, S.I. Didenko, et al., Trap states in multication mesoscopic perovskite solar cells: A deep levels transient spectroscopy investigation, Appl. Phys. Lett. 113 (2018) 263501. doi:10.1063/1.5053845.

[54] V. Campanari, A. Agresti, S. Pescetelli, A.K. Sivan, D. Catone, P. O'Keeffe, et al., Systematic approach to the study of the photoluminescence of MAPb I3, Phys. Rev. Mater. 5 (2021) 1–10. doi:10.1103/PhysRevMaterials.5.035409.

[55] D. Saranin, P. Gostischev, D. Tatarinov, I. Ermanova, V. Mazov, D. Muratov, et al., Copper iodide interlayer for improved charge extraction and stability of inverted perovskite solar cells, Materials (Basel). 12 (2019) 1–14. doi:10.3390/ma12091406.

[56] W. Chen, Y. Wu, Y. Yue, J. Liu, W. Zhang, X. Yang, et al., Efficient and stable large-area perovskite solar cells with inorganic charge extraction layers, Science (80-.). 350 (2015) 944–948. doi:10.1126/science.aad1015.

[57] J. Shi, Y. Li, Y. Li, D. Li, Y. Luo, H. Wu, et al., From Ultrafast to Ultraslow: Charge-Carrier Dynamics of Perovskite Solar Cells, Joule. 2 (2018) 879–901. doi:10.1016/j.joule.2018.04.010.

[58] P. Lopez-Varo, J.A. Jiménez-Tejada, M. García-Rosell, S. Ravishankar, G. Garcia-Belmonte, J. Bisquert, et al., Device Physics of Hybrid Perovskite Solar cells: Theory and Experiment, Adv. Energy

Mater. 8 (2018). doi:10.1002/aenm.201702772.

[59] A. Agresti, B. Berionni Berna, S. Pescetelli, A. Catini, F. Menchini, C. Di Natale, et al., Copper-Based Corrole as Thermally Stable Hole Transporting Material for Perovskite Photovoltaics, Adv. Funct. Mater. 30 (2020) 1–11. doi:10.1002/adfm.202003790.

[60] L. Gouda, R. Gottesman, A. Ginsburg, D.A. Keller, E. Haltzi, J. Hu, et al., Open Circuit Potential Build-Up in Perovskite Solar Cells from Dark Conditions to 1 Sun, J. Phys. Chem. Lett. 6 (2015) 4640–4645. doi:10.1021/acs.jpclett.5b02014.

[61] S. Shao, Z. Chen, H.H. Fang, G.H. Ten Brink, D. Bartesaghi, S. Adjokatse, et al., N-type polymers as electron extraction layers in hybrid perovskite solar cells with improved ambient stability, J. Mater. Chem. A. 4 (2016) 2419–2426. doi:10.1039/c5ta10696f.

[62] G. Zanotti, N. Angelini, G. Mattioli, A.M. Paoletti, G. Pennesi, D. Caschera, et al., [1]Benzothieno[3,2-b][1]benzothiophene-Phthalocyanine Derivatives: A Subclass of Solution-Processable Electron-Rich Hole Transport Materials, Chempluschem. 85 (2020) 2376–2386. doi:10.1002/cplu.202000281.

[63] N. Ahn, K. Kwak, M.S. Jang, H. Yoon, B.Y. Lee, J.K. Lee, et al., Trapped charge-driven degradation of perovskite solar cells, Nat. Commun. 7 (2016) 1–9. doi:10.1038/ncomms13422.

[64] M.C. Brennan, A. Ruth, P. V. Kamat, M. Kuno, Photoinduced Anion Segregation in Mixed Halide Perovskites, Trends Chem. 2 (2020) 282–301. doi:10.1016/j.trechm.2020.01.010.

[65] Z. Andaji-Garmaroudi, M. Abdi-Jalebi, D. Guo, S. Macpherson, A. Sadhanala, E.M. Tennyson, et al., A Highly Emissive Surface Layer in Mixed-Halide Multication Perovskites, Adv. Mater. 31 (2019). doi:10.1002/adma.201902374.

[66] S. Cacovich, D. Messou, A. Bercegol, S. Béchu, A. Yaiche, H. Shafique, et al., Light-induced passivation in triple cation mixed halide perovskites: Interplay between transport properties and surface chemistry, ACS Appl. Mater. Interfaces. 12 (2020) 34784–34794. doi:10.1021/acsami.0c06844.

[67] A.L. Palma, F. Matteocci, A. Agresti, S. Pescetelli, E. Calabro, L. Vesce, et al., Laser-Patterning Engineering for Perovskite Solar Modules With 95% Aperture Ratio, IEEE J. Photovoltaics. 7 (2017) 1674–1680. doi:10.1109/JPHOTOV.2017.2732223.

[68] S. Razza, S. Pescetelli, A. Agresti, A. Di Carlo, Laser Processing Optimization for Large-Area Perovskite Solar Modules, Energies. 14 (2021) 1069. doi:10.3390/en14041069.

[69] R. Wang, M. Mujahid, Y. Duan, Z.-K. Wang, J. Xue, Y. Yang, A Review of Perovskites Solar Cell Stability, Adv. Funct. Mater. 1808843 (2019) 1808843. doi:10.1002/adfm.201808843.

[70] S. Kundu, T.L. Kelly, In situ studies of the degradation mechanisms of perovskite solar cells, EcoMat. 2 (2020) 1–22. doi:10.1002/eom2.12025.

[71] M. Spalla, L. Perrin, E. Planes, M. Matheron, S. Berson, L. Flandin, Effect of the Hole Transporting/Active Layer Interface on the Perovskite Solar Cell Stability, ACS Appl. Energy Mater. 3 (2020) 3282–3292. doi:10.1021/acsaem.9b02281.

[72] D. Catone, G. Ammirati, P.O. Keeffe, F. Martelli, L. Di Mario, S. Turchini, et al., Mixed-Cation Hybrid Lead Halide Perovskites, Energies. 14 (2021) 708–722.